remote sensing

MDPI

Article

Analysis of the Spatial and Temporal Evolution of Land Subsidence in Wuhan, China from 2017 to 2021

Yizhan Zhao [1], Lv Zhou [1,*], Cheng Wang [1,2], Jiahao Li [1], Jie Qin [3], Haiquan Sheng [1], Liangke Huang [1] and Xin Li [4,5]

[1] College of Geomatics and Geoinformation, Guilin University of Technology, Guilin 541004, China; zhaoyizhan@glut.edu.cn (Y.Z.); bx20211013@glut.edu.cn (C.W.); lijiahao@glut.edu.cn (J.L.); 3202080807117@glut.edu.cn (H.S.); lkhuang@whu.edu.cn (L.H.)
[2] Guangxi Institute of Natural Resources Survey and Monitoring, Nanning 530023, China
[3] Natural Resources and Real Estate Registration Center of Guangxi Zhuang Autonomous Region, Nanning 530029, China; 3182042041826@glut.edu.cn
[4] Guangxi Key Laboratory of Spatial Information and Geomatics, Guilin University of Technology, Guilin 541004, China; lixin2017@chd.edu.cn
[5] College of Geology Engineering and Geomantic, Chang'an University, Xi'an 710054, China
* Correspondence: zhoulv@glut.edu.cn

Abstract: Land subsidence is a common geological hazard. Rapid urban expansion has led to different degrees of ground subsidence within Wuhan in the past few years. The novel coronavirus outbreak in 2020 has seriously impacted urban construction and people's lives in Wuhan. Land subsidence in Wuhan has changed greatly with the resumption of work and production. We used 80 Sentinel-1A Synthetic Aperture Radar (SAR) images covering Wuhan to obtain the land subsidence change information of Wuhan from July 2017 to September 2021 by using the small baseline subset interferometric SAR technique. Results show that the subsidence in Wuhan is uneven and concentrated in a few areas, and the maximum subsidence rate reached 57 mm/yr during the study period. Compared with land deformation before 2017, the land subsidence in Wuhan is more obvious after 2020. The most severe area of subsidence is located near Qingling in Hongshan District, with a maximum accumulated subsidence of 90 mm, and obvious subsidence funnels are observed in Qiaokou, Jiangan, Wuchang and Qingshan Districts. The location of subsidence centers in Wuhan is associated with building intensity, and most of the subsidence funnels are formed in connection with urban subway construction and building construction. Carbonate belt and soft ground cover areas are more likely to lead to karst collapse and land subsidence phenomena. Seasonal changes are observed in the land subsidence in Wuhan. A large amount of rainfall can replenish groundwater resources and reduce the rate of land subsidence. The change in water level in the Yangtze River has a certain impact on the land subsidence along the rivers in Wuhan, but the overall impact is small. An obvious uplift is observed in Caidian District in the south of Wuhan, and the reason may be related to the physical and chemical expansion effects of the expansive clay.

Keywords: land subsidence; SBAS-InSAR; Wuhan city; urban construction; land uplift

Citation: Zhao, Y.; Zhou, L.; Wang, C.; Li, J.; Qin, J.; Sheng, H.; Huang, L.; Li, X. Analysis of the Spatial and Temporal Evolution of Land Subsidence in Wuhan, China from 2017 to 2021. *Remote Sens.* **2022**, *14*, 3142. https://doi.org/10.3390/rs14133142

Academic Editors: Guohong Zhang, Chisheng Wang, Wu Zhu, Daqing Ge and Siting Xiong

Received: 27 May 2022
Accepted: 27 June 2022
Published: 30 June 2022

1. Introduction

Land subsidence is a geological phenomenon of regional ground elevation reduction caused by natural or human factors [1–3]. With rapid urban expansion and excessive groundwater extraction, it has become a widespread geohazard in many cities worldwide [4,5]. Many countries and regions in the world, such as Iran, Italy, Egypt, Spain, Mexico and Texas, are facing the problem of land subsidence [6–12]. Among them, Jakarta, the capital of Indonesia, had to move its capital to East Kalimantan Province due to severe land subsidence [13]. Subsidence can decrease the water storage capacity of underground aquifers, leading to land collapse, damage to buildings and civil infrastructures, and increased risk of flooding [14–16]. The United Nations has studied and predicted that the

global land subsidence will affect 1.6 billion residents by 2040 [17]. Therefore, subsidence in large cities must be monitored.

As the largest developing country in the world, China is experiencing a large-scale and high-speed urbanization. Land subsidence caused by excessive exploitation of groundwater and high-intensity urban construction is becoming increasingly exacerbated. For example, land subsidence has occurred in Beijing, Tianjin, Guangdong, Foshan and other cities [18–22]. Statistics show that the area where ground subsidence of more than 10 mm/yr occurs in China is more than 120,000 km^2 by the end of 2015, involving 94 prefecture-level cities and 425 districts and counties [23]. Wuhan is a central city in the central region of China and is the political, economic and cultural center of Hubei Province. In recent years, Wuhan is on a speed way of urbanization and rail transit construction. At present, the permanent resident population of Wuhan has reached 12.33 million, and the operating mileage of rail transit has reached 409.1 km. Large-scale urban construction and the special geological structure of Wuhan often lead to land subsidence caused by karst collapse, soft soil compression and engineering construction [24,25].

The first recorded land surface subsidence in Wuhan occurred in 1931 [26]. With the increase in human activities and the overexploitation of groundwater, the rate and extent of subsidence in Wuhan are increasing [27,28]. In particular, the rapid expansion of Wuhan in recent years has led to the emergence of several subsidence funnels within the city. Land subsidence can be divided into three types: tectonic subsidence caused by crustal subsidence movement, pumping subsidence and goaf subsidence [29]. The main causes of ground subsidence in Wuhan are the consolidation of soft soil layers and karst ground collapse caused by groundwater overdraft and urban construction [30,31]. Monitoring land subsidence in Wuhan mainly depends on about 300 benchmark points distributed in the city but lacks long-term effective land subsidence monitoring [32]. Although traditional measurement techniques (e.g., level survey and global navigation satellite system) have high measurement accuracy and sensitivity, performing subsidence monitoring on a large scale is difficult [33,34]. Interferometric Synthetic Aperture Radar (InSAR) technology can compensate for the shortcomings of traditional deformation monitoring methods [35,36]. Specifically, the time series InSAR technology overcomes the problems of temporal and spatial decorrelation and atmospheric effect [37,38] and greatly improves the measurement accuracy. This method has been widely used in the fields of land subsidence and landslide monitoring [39–42]. The often-used time series InSAR techniques include Persistent Scatterer InSAR (PS-InSAR), Small Baseline Subset InSAR (SBAS-InSAR) and Multi-Temporal InSAR (MT-InSAR) [43–45].

Bai et al. [46] first monitored the Wuhan urban area using high-resolution TerraSAR-X data and found that the land deformation rate in Wuhan ranges from −64 to 18 mm/yr between 2009 and 2010, with Hankou being the largest subsidence area, and urban construction and karst geology being the major causative factors of subsidence. Costantini et al. [47] used COSMO-SkyMed SAR data to obtain the land deformation rates in Hankou from 2013 to 2014 ranging from −80 to 40 mm/yr. Urban construction in Wuhan accelerated after 2015, and approximately 10,000 sites were under construction, leading to serious land subsidence and collapse in the city [48–51]. Zhou et al. found land subsidence was the most severe in the Houhu area between 2015 and 2016, with a maximum subsidence rate of more than 80 mm/yr [49]. Zhang et al. found that subsidence had occurred in Hankou, Wuchang, Hanyang, Qingshan Industrial Park and Baishazhou between 2015 and 2018 [51].

In this study, we used the SBAS-InSAR technique to obtain the surface deformation of Wuhan between July 2017 and September 2021. Here, we discussed the relationship between land subsidence and rainfall, the total amount of groundwater and the change in river level, which can provide a reference for the prevention of land subsidence disasters in Wuhan.

2. Study Area and Datasets

2.1. Study Area

Wuhan is located in the eastern part of Hubei Province (South East China) and it covers an area of 8494.41 km^2. It is situated at the intersection of hills, mountains and the Han River Plain, as shown in Figure 1a. The overall topography is high in the south and low in the north, with a remnant mounded impact plain in the middle. Wuhan has a maximum West–East directional distance of 134 km from east to west and a maximum North–South directional distance of about 155 km (at latitude 29°58′N to 31°22′N and longitude 113°41′E to 115°05′E) with altitudes ranging from 19.2 m to 873.7 m. Wuhan has a north subtropical monsoonal (humid) climate with rainfall concentrated between June and August each year, and is characterized by rain and heat in the same season and four distinctive seasons [52,53]. Many rivers and lakes form in the city, where the Yangtze River and Han River form a huge water network. The total water area reaches 2217.6 km^2, accounting for about 26.1% of the city's total area.

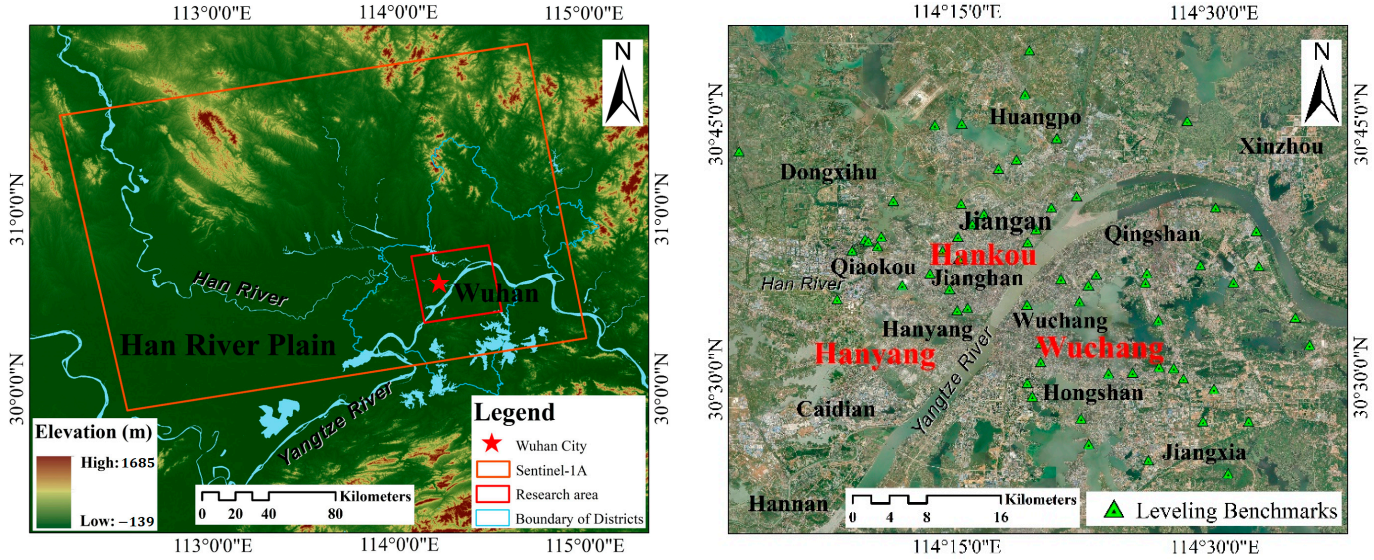

Figure 1. (**a**) Geographical location of Wuhan. The orange rectangle illustrates the coverage of Sentinel-1A, and the red rectangle is the study area. (**b**) Optical satellite image of Wuhan, where green triangles indicate level benchmarks.

Wuhan has several belts of occult carbonates, consisting of the "Lower Carbonate Group" with a total thickness of more than 200 m deposited in the middle of the Late Paleozoic and the "Upper Carbonate Group" represented by marl, thin-bedded tuff, thick-bedded tuff and thick-bedded dolomite deposited in the Early Triassic. The Indochinese movement at the end of the Middle Triassic forged the basic outline of the carbonate stratigraphy in Wuhan [54]. As shown in Figure 2, the carbonate rock group is distributed in a plane from north to south, forming a total of six carbonate belts (L1–L6). Wuhan is located at the intersection of the Yangtze River and the Han River [30]. The soft soil is mainly silty soil and silt, and it has a large distribution in the sections along the rivers and around the lakes in Hankou, Wuchang, Hannan, Xinzhou and Jiangxia, with a maximum thickness of 37 m and a minimum thickness of 0.1 m. The soft soil with low strength and high compressibility covers most areas of the city and is easy to cause foundation settlement and other adverse geological problems [28]. The complex geological structure often leads to disaster events, such as sinkholes, uneven foundation settlements and landslides, in Wuhan [26,30].

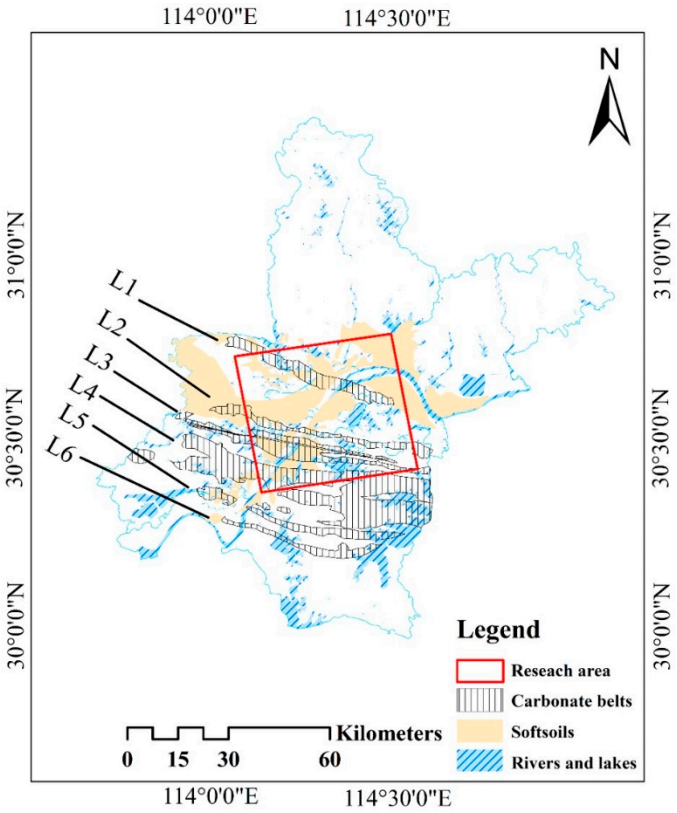

Figure 2. Geological structure map of Wuhan. Carbonate belts (L1–L6) are the Tianxingzhou karst belt, Bridge karst belt, Baishazhou karst belt, Zhuankou karst belt, Junshan karst belt and Hannan karst belt, respectively.

2.2. Datasets

We employ 80 ascending Sentinel-1A single-look complex images acquired from July 2017 to September 2021. These images cover the entire area of Wuhan, with a 1-month interval for image acquisition between July 2017 and December 2019 and a 12-day interval for images between January 2020 and September 2021. The information of Sentinel-1A images is shown in Table 1. We used the Shuttle Radar Topography Mission (SRTM) 30 m Digital Elevation Model by the National Aeronautics and Space Administration to remove topographic phases, and precise orbit ephemerides provided by the European Space Agency to eliminate orbital errors.

Table 1. Specific parameters of Sentinel-1A data.

Parameter	Value	Parameter	Value
Product type	Sentinel-1A	Incidence angle	39°
Wavelength	C-band	Path	113
Flight direction	Ascending	Resolution	2.7 m × 22 m
Polarization	VH	Number of images	80
Beam mode	IW	Time range	17 July 2017–30 September 2021

We collected some data related to ground subsidence in Wuhan. Wuhan Metro information is obtained from Wuhan Metro Group Co., Ltd., Wuhan, China. The distribution map of soft soil and carbonate rocks is acquired from Hubei Geological Bureau. Rainfall and groundwater data are obtained from the Wuhan Water Resources Bulletin. The water level information comes from the Water Resources Department of Hubei Province

(https://slt.hubei.gov.cn, accessed on 29 December 2021). To more intuitively analyze the urban changes in Wuhan, we used Google Earth historical optical images.

3. Methods

3.1. SBAS-InSAR Technique

SBAS-InSAR technology combines the data into several sets in accordance with the distribution of SAR image sequences in temporal and spatial baselines. Within the set, the interferometric image is smaller for the spatial baseline, and the interferometric image is larger for the spatial baseline between the sets, resulting in a small baseline interferogram. On the basis of the minimum norm criterion of deformation rate, the deformation rate and its time series of the coherent target are obtained by using the least square method or Singular Value Decomposition (SVD) [44].

If the target feature has $N+1$ SAR images, then time to acquire the image is $t_0 \sim t_N$. Images from the same area at different times can interfere with each other, and two images can be found in at least one subset. One of the images is selected as the master image, and the remaining images are registered with it. N view images can generate M multi-view differential interferograms, and M satisfies the following inequality [48]:

$$\frac{N+1}{2} \leq m \leq N\left(\frac{N+1}{2}\right) \tag{1}$$

The differential interferogram j is generated by interfering the SAR image maps at time t_A and time t_B ($t_B > t_A$). The extracted high coherence points are phase unwrapped after removing the flat-earth and topographic phase, and the phase of the differential interferogram at pixel coordinates (x, r) can be expressed as:

$$\begin{aligned} &\delta\phi_j(x,r) = \phi(t_B,x,r) - \phi(t_A,x,r) \\ &\approx \tfrac{4\pi}{\lambda}[d(t_B,x,r) - d(t_A,x,r)] + \Delta\phi^j_{topo}(x,r) + \Delta\phi^j_{APS}(t_B,t_A,x,r) \\ &+\Delta\phi^j_{noise}(x,r) \end{aligned} \tag{2}$$

where $\phi(t_A,x,r)$ and $\phi(t_B,x,r)$ represent the phase values of SAR images at t_A and t_B, respectively, $d(t_B,x,r)$ and $d(t_A,x,r)$ are the cumulative form variables in the Line of Sight (LOS) direction relative to $d(t_0,x,r)$ at moments t_B and t_A. $\Delta\phi^j_{topo}(x,r)$ denotes the residual phase of the differential interferogram. $\Delta\phi^j_{APS}(t_B,t_A,x,r)$ is the phase error caused by atmospheric delay. $\Delta\phi^j_{noise}(x,r)$ denotes random noise phases.

When the effect of error is ignored, Equation (2) can be simplified as:

$$\delta\phi_j(x,r) = \phi(t_B,x,r) - \phi(t_A,x,r) \approx \frac{4\pi}{\lambda}[d(t_B,x,r) - d(t_A,x,r)] \tag{3}$$

The phase in Equation (3) is expressed as the product of the average phase rate and time between the two acquisition times to obtain the settlement time series with physical meaning:

$$v_j = \frac{\phi_j - \phi_{j-1}}{t_j - t_{j-1}} \tag{4}$$

The phase value of the interferogram j can be written as:

$$\sum_{k=t_A,j+1}^{t_B,j} (t_k - t_{k-1})v_k = \delta\phi_j \tag{5}$$

This equation indicates that the integration of the rate of each time period over the master and slave image time intervals is expressed in matrix form as:

$$B\nu = \delta\phi \tag{6}$$

Rank deficiency is likely to occur because the SBAS-InSAR technique uses multiple master image spatio-temporal baselines to obtain differential interference. The generalized inverse matrix of matrix B can be obtained by using SVD to acquire the minimum norm solution of rate vector. The rate in each time period is integrated to obtain the amount of surface settlement in each time period.

3.2. SBAS-InSAR Data Processing

The main processing flow of SBAS-InSAR method is shown in Figure 3, which mainly includes the steps of generating small baseline subsets, interferogram formation and phase unwrapping, refinement and reflattening, and generation time series results. To more intuitively compare the changes in subsidence in Wuhan before and after the COVID-19, this study divides the data into two time periods (July 2017 to June 2020 and January 2020 to September 2021). The two time periods have half year data overlap to ensure the continuity of settlement results [49].

(1) Generating connection pairs: we selected the images of 13 January 2018 and 18 August 2020 as the master images and realigned the other images with the master images to avoid the effect of temporal and spatial decorrelation factors. For the first time period, the time threshold is 180 days, and the spatial baseline threshold is 45%. In the second time period, the time threshold is 60 days, and the critical value of spatial baseline is 45%.
(2) Interferogram formation and phase unwrapping: interference processing is performed on all interferometric pairs to generate differential interferograms, remove the flat-earth and topographic phase, perform phase unwrapping and generate phase diagram.
(3) Refinement and reflattening: this process mainly aims to estimate and remove the residual phases and ramp phase that still exists after phase unwrapping.
(4) Generation of time series results: the phase after unwrapping is calculated by using SVD, and the atmospheric phase and other errors are removed by two inversions to obtain the accurate displacement results on the time series. The final deformation value in the LOS direction is obtained by geocoding.

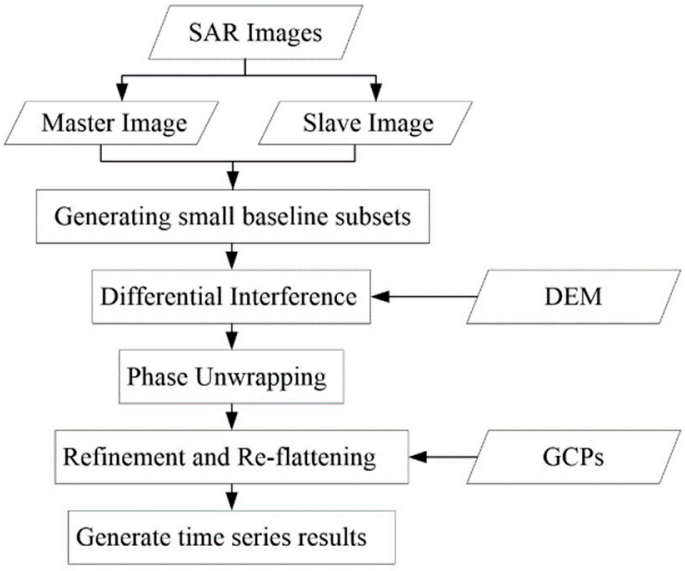

Figure 3. SBAS flow chart.

4. Results

4.1. Temporal and Spatial Distribution Characteristics of Land Subsidence in Wuhan

Figures 4 and 5 show the land subsidence rates in the LOS direction in Wuhan for the two time periods, respectively. Positive values in the graph indicate land uplift, whereas negative values indicate land subsidence. We extracted 2,851,137 PS points in the study area using SBAS InSAR technique from July 2017 to June 2020 (Figure 4), and the deformation rate in the main urban area of Wuhan ranged from −46.2 mm/yr to 24.6 mm/yr during the study period, with an average subsidence rate of 0.3 mm/yr. Four subsidence areas are found Qiaokou, Jiang'an, Qingshan and Hongshan Districts. The subsidence in Qingshan District is relatively serious, which may be related to the presence of a large number of industrial parks in the area, such as Wuhan Iron and Steel (Group) Company and Wuhan Petrochemical Plant.

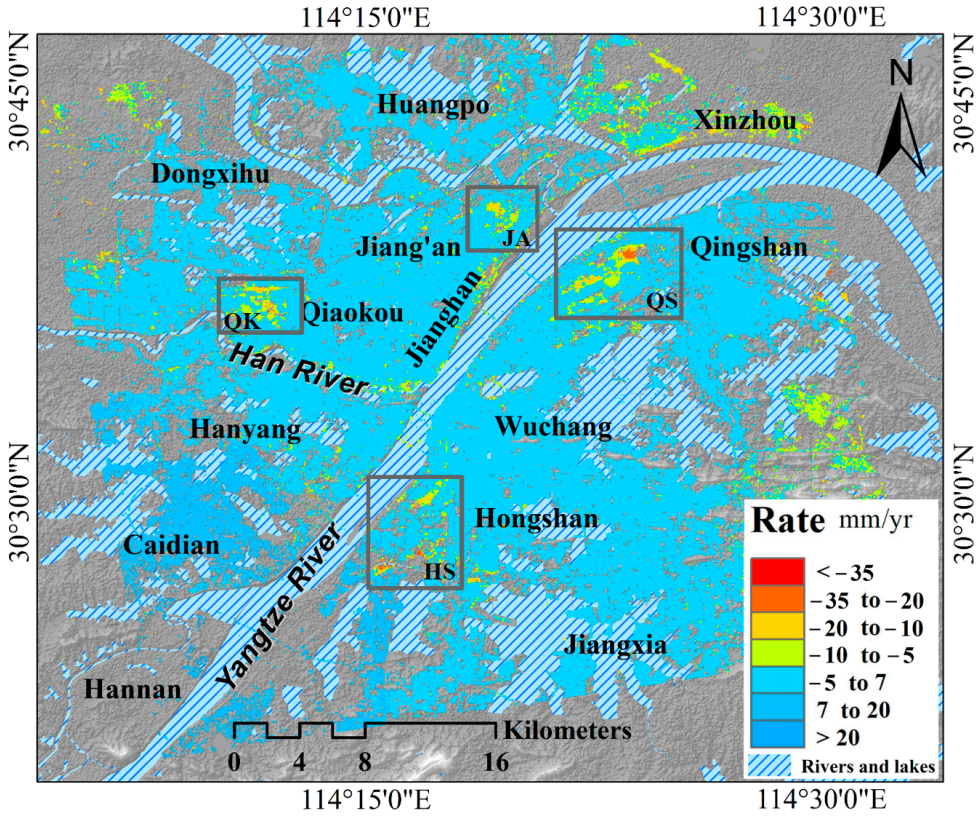

Figure 4. Land subsidence rate in the LOS direction in Wuhan from July 2017 to June 2020. The gray rectangles are the major areas of subsidence. JA, QK, QS and HS are the abbreviations of Jiangan, Qiaokou, Qingshan and Hongshan, respectively.

A total of 4,375,472 PS points were acquired from January 2020 to September 2021 (Figure 5), and the deformation rate varies from −57.1 mm/yr to 33.1 mm/yr with an average of −2.2 mm/yr. The subsidence in Wuhan has a high tendency to further expand after 2020. Five obvious subsidence areas are found in the main urban area: Jiangan, Qiaokou, Qingshan, Wuchang and Hongshan Districts. Compared with previous results, Qingshan District has a large-scale settlement phenomenon, and the settlement center is located in the Wuhan Iron and Steel (Group) Company (WISCO) ironmaking plant. The subsidence near Qingling in Hongshan District is the most serious, and the land subsidence rate in some areas exceeds 50 mm/yr under the influence of urban and subway construction. The overall subsidence range in Wuhan is small, and the deformation rate in most areas is between −5 mm/yr and 7 mm/yr. Land subsidence in Wuhan is concentrated in a few areas. Interestingly, uplift has been occurring in parts of Caidian District in the southern part of Wuhan.

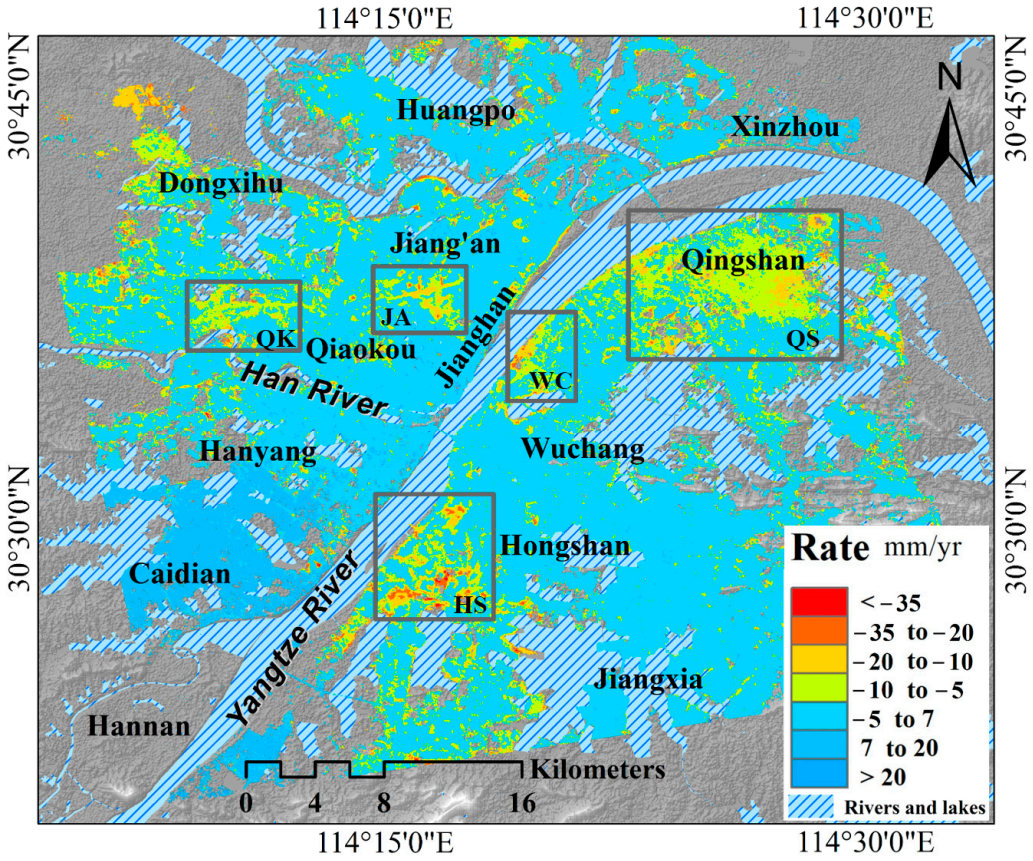

Figure 5. Land subsidence rate in the LOS direction in Wuhan from January 2020 to September 2021. The gray rectangles indicate the major area of subsidence. JA, QK, QS, WC and HS are the abbreviations of Jiangan, Qiaokou, Qingshan, Wuchang and Hongshan, respectively.

To explore the temporal evolution of land subsidence in Wuhan, we used the image acquired on 3 January 2020, as the reference image for the time series and calculated the time series of cumulative subsidence in Wuhan from 3 January 2020 to 30 September 2021. The results are shown in Figure 6. The distribution of cumulative settlement is consistent with the distribution of subsidence rate, which is relatively stable in most areas of Wuhan city, with cumulative settlement mostly between −5 and 10 mm. The maximum subsidence in Wuhan during the study period is 104 mm, located near Qingling, Hongshan District. The settlement in the main subsidence zone gradually increases with time, and the area of the subsidence funnel gradually expands. Land subsidence in Wuhan can be significantly nonlinear with seasonal changes. The area of subsidence increases rapidly between March and June during the same year. However, the change in subsidence is smaller between June and September, and a slowing trend is observed in land subsidence. Land subsidence may be influenced by rainfall. Wuhan has a considerable amount of rainfall from June to August, and a large amount of rainfall can effectively recharge groundwater, which may alleviate the land subsidence.

To check the accuracy of the Wuhan land subsidence results obtained by SBAS-InSAR technique, we evaluated the error of the average deformation rate in two time periods. The Root Mean Square Error (RMSE) is obtained by calculating the deviation of rate linear fitting. The probability density function of the RMSE of subsidence rate in the two time periods is shown in Figure 7a,b, and the average value of RMSE is 2.5 and 2.6 mm/yr, respectively. The RMSE of 97% PS points in the study area is less than 5 mm/yr, which has high accuracy for InSAR time series results.

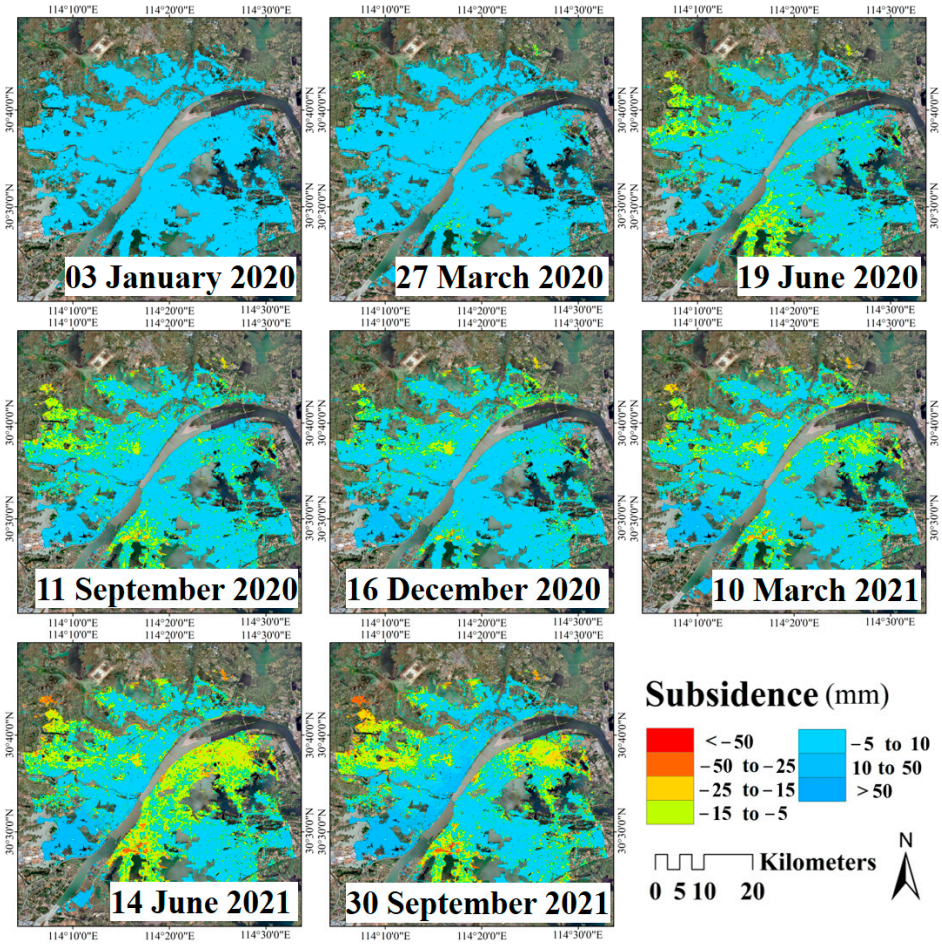

Figure 6. Time series of cumulative settlement from 3 January 2020 to 30 September 2021. The image obtained on 3 January 2020 is the reference image.

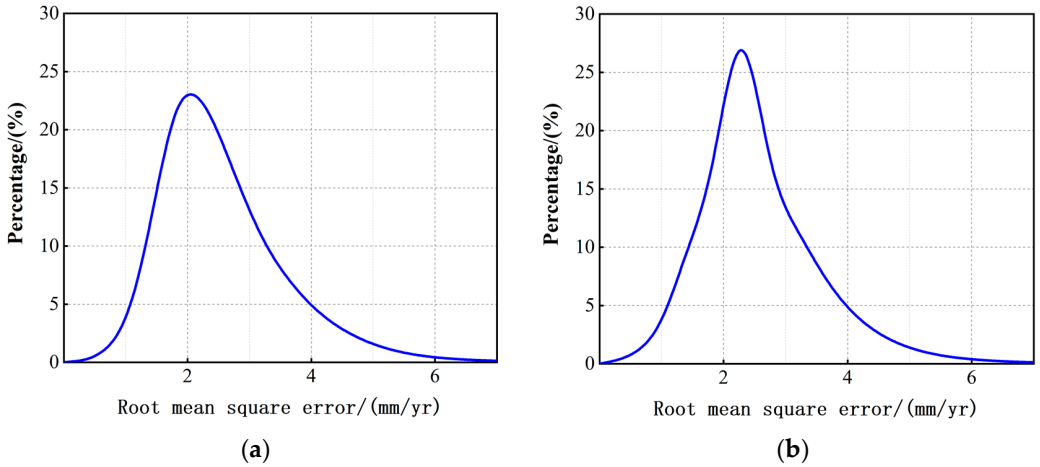

Figure 7. (**a**) RMSE of subsidence results from 17 July 2017 to 19 June 2020; (**b**) RMSE of subsidence results from 3 January 2020 to 30 September 2021.

4.2. Subsidence Changes before and after the COVID-19 in Wuhan

The changes in the main subsidence areas in Wuhan are shown in Figure 8. Five major areas of subsidence are found in Wuhan between June 2017 and September 2021, with the degree and extent of subsidence increasing in each area over time. The subsidence area in Jiangan District (JA) transfers from north to south, and the subsidence is mainly concentrated near Hankou Railway Station with the maximum subsidence rate around

30 mm/yr. The subsidence in Qiaokou (QK) District gradually transfers westward with time, and the subsidence along the Han River is more serious. A severe subsidence funnel occurred near Heping Avenue in Qingshan District (QS) between 2017 and 2020, and the subsidence of this funnel decreased after 2020. However, a widespread subsidence phenomenon occurred in the central part of Qingshan District (QS) compared with the previous period, with the deformation rate ranging from −40 mm/yr to −20 mm/yr. The Wuchang District experienced a subsidence after 2020, with severe subsidence occurring in areas close to the Yangtze River. The subsidence in Hongshan (HS) District is the most severe. Many areas have severe subsidence, and they are becoming contiguous.

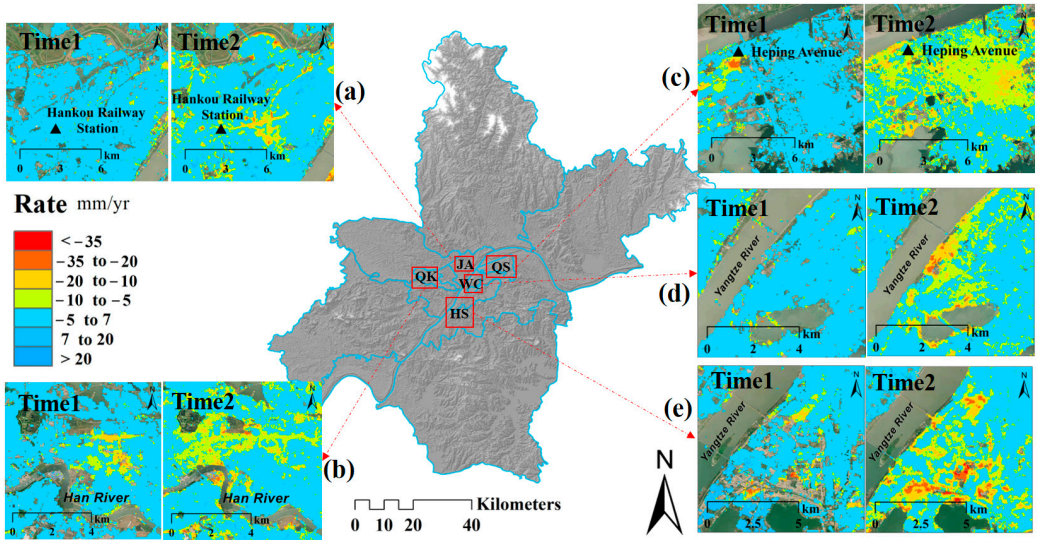

Figure 8. Changes in major subsidence areas in Wuhan from 17 June 2017 to 30 September 2021. The red rectangles are the five detected subsidence areas. Time 1 indicates June 2017 to June 2020, and time 2 denotes January 2020 to September 2021. JA, QK, QS, WC and HS are the abbreviations of Jiangan, Qiaokou, Qingshan, Wuchang, and Hongshan, respectively. The black triangle in (**a**) indicates the location of Hankou Railway Station, and the black triangle in (**b**) indicates the location of Heping Avenue. (**a**–**e**) indicate the sudsidence changes in Jiangan, Qiaokou, Qingshan, Wuchang and Hongshan, respectively.

We conducted a statistical analysis of the subsidence rate in Wuhan to analyze the subsidence changes in recent years. We calculated the percentage of PS points in different deformation rate ranges when performing the comparative analysis due to the large difference in the number of PS points in the two results. The results are shown in Figure 9a. The percentage of the PS points after the COVID-19 is higher than that before the COVID-19 in each range of deformation rate. A large change is observed in the number of PS points in the deformation rate ranging from −15 mm/yr to −5 mm/yr, and the percentage increases from 6.86 to 33.21%, which indicates a large-scale subsidence phenomenon in Wuhan after 2020. The number of PS points within the deformation rate ranging from −25 mm/yr to 15 mm/yr increases significantly, indicating that the subsidence situation in Wuhan is aggravated.

Figure 9b,c show the changes in the maximum and average deformation rates for the five major subsidence areas in Wuhan, respectively. The average deformation rate of Qingshan and Hongshan Districts changes the most due to a large-scale subsidence phenomenon in Qingshan District, and the subsidence phenomenon in Hongshan District is intensified. The maximum subsidence rate of each area exceeds 20 mm/yr between June 2017 and September 2021. After 2020, the deformation rate increases in all regions, with the maximum subsidence rate in Hongshan District exceeding 50 mm/yr.

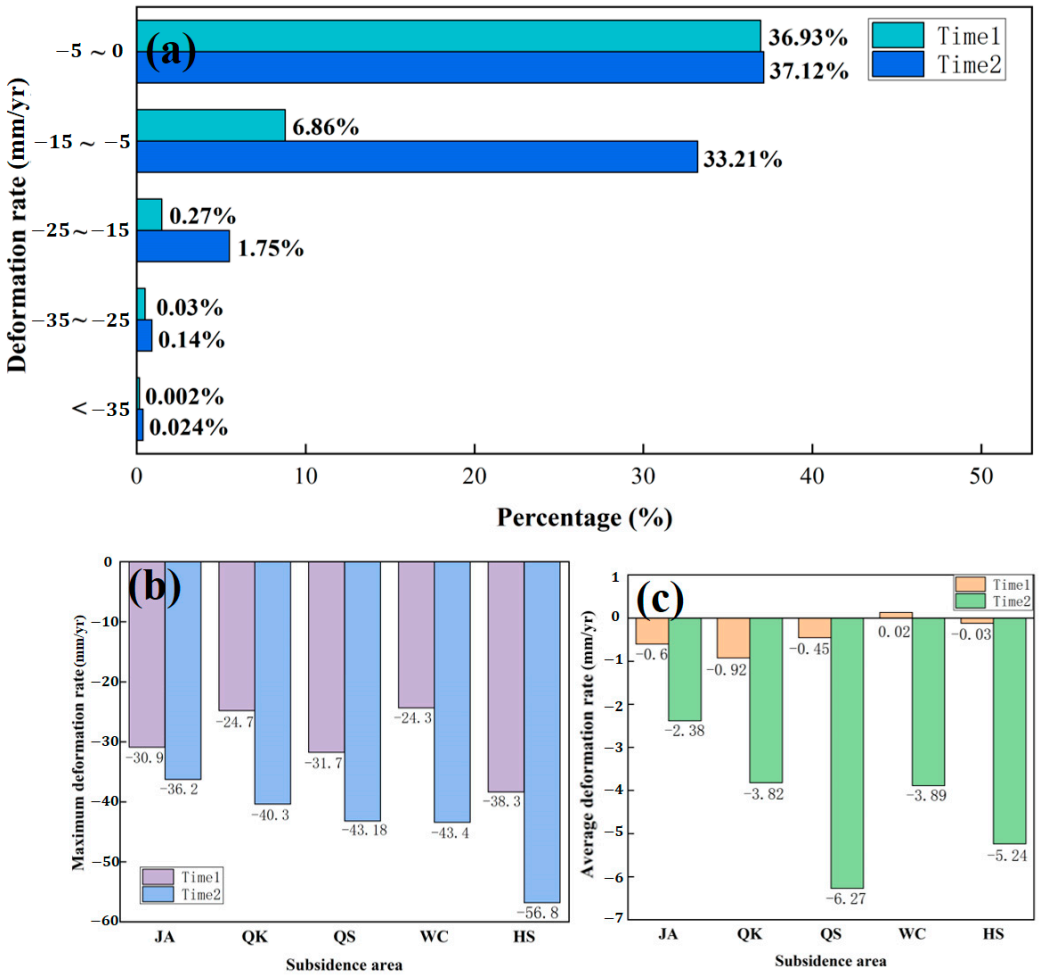

Figure 9. (**a**) Percentage of different deformation rate intervals; (**b**) changes in the maximum deformation rate of the major subsidence areas; (**c**) changes in the average deformation rate of the major subsidence areas. Time 1 denotes June 2017 to June 2020, and time 2 indicates January 2020 to September 2021.

In this study, we obtained the land subsidence results of Wuhan city in the last 4 years from 2017 to 2021. We summarized the results of previous studies on land subsidence monitoring in Wuhan to study the early subsidence, as shown in Table 2. The early subsidence funnels in Wuhan are distributed in Hankou, Qingshan, Wuchang and near Baishazhou, and the most obvious subsiding area is located in Houhu [46,47]. Historically, Houhu is a lake beach, and the lower cushion is composed of silt with a thickness of 10 m to 30 m. Urban development, especially the continuous construction of super high-rise buildings, has caused great pressure on the soft soil foundation. Previous studies showed that the Houhu area experienced severe subsidence between 2013 and 2016, with the maximum subsidence rate exceeding 80 mm/yr [48]. Qingshan District is the industrial center of Wuhan. A large amount of groundwater has been extracted because of industrial activities, resulting in land subsidence in the Qingshan District. In summary, the subsidence in Wuhan has been alleviated since 2017. The subsidence in the Houhu area has mitigated significantly, and the subsidence in other areas has also been alleviated [49]. However, the subsidence phenomenon in Wuhan intensified after 2020, with several areas experiencing subsidence [51].

Table 2. Summary of the previous studies of land subsidence in Wuhan.

Study	Method	Dataset	Deformation Rate	Main Subsidence Area
Bai et al. (2016) [46]	PS-InSAR	12 TerraSAR images (October 2009–August 2010)	−67 to 17.5 mm/yr	The largest subsidence area in Wuhan is located in Hankou
Costantini et al. (2016) [47]	PSP-InSAR approach	45 Cosmo-SkyMed images (June 2013–June 2014)	−80 to 40 mm/yr	Most areas of Hankou
Zhou et al. (2017) [48]	SBAS-InSAR	15 Sentinel-1 images (Aprirl 2015–April 2016)	−82 to 18 mm/yr	Houhu, Wuchang, Hanyang, Qingshan
Zhang et al. (2019) [49]	SBAS-InSAR	20 Radarsat-2 images (October 2015–June 2018)	−52 to 28 mm/yr	Houhu, Qingshan Industrial Park, Baishazhou
Shi et al. (2021) [51]	SBAS-InSAR	113 Sentinel-1 Images (April 2015–September 2019)	−30 to 30 mm/yr	Qingshan, Houhu, Dongxihu, Qingling

5. Discussion

Many factors are associated with the subsidence of Wuhan. Next, we will discuss the causes of land subsidence in Wuhan in terms of subway construction, urban infrastructure construction, hydrogeology, groundwater and rainfall, and river level changes. We will also briefly analyze the ground uplift phenomenon in Caidian District.

5.1. Subway Construction

Subways can effectively alleviate the pressure of urban ground traffic and improve commuting efficiency. However, subway tunneling can affect the surrounding soil during subway construction and cause ground deformation. In the area of dense buildings, subway tunneling can even lead to foundation deformation, affecting the safety of subway construction and ground buildings. Wuhan started to build subways as early as 2000. The total number of subway operating mileage in Wuhan reached 435 km with 14 subway lines by the end of 2021. The distribution of subway is shown in Figure 10a. To investigate the relationship between subway construction and land subsidence, we extracted the land subsidence within 500 m on two sides of the subway (Figure 10b). We counted the information of subway lines under construction in Wuhan during the study period, as shown in Table 3. The findings indicate that the land subsidence along Metro Line 5 is relatively severe, with the subsidence rate exceeding 35 mm/yr in some areas, and some sections of Metro Lines 6 and 12 have experienced subsidence exceeding 20 mm/yr. Two typical subsidence areas are located near Qingling Station in Hongshan District (HS) and Shiqiao Station in Jiangan District (JA).

The subsidence in the area near Qingling Station is shown in Figure 11a, with several subsiding areas along the elevated bridge section of Metro Line 5. The construction of Wuhan Metro Line 5 is difficult due to the access to the Qingling River, the elevated Third Ring Road and the karst area. A part of the line passes through the main traffic road in Baishazhou, and the surrounding communities are dense, so subsidence is extremely easy to occur during construction. Wuhan Metro Line 5 returned to construction on 24 March 2020. As a transit station for Metro Lines 5 and 12, Qingling Station has a large land subsidence. In this study, we conducted a profile analysis along the Qingling Station of Line 5 (black dashed line AA' in the figure). Figure 11b,c indicate the profile deformation rate and cumulative settlement, respectively. The subsidence fluctuation shows an "M" shape, with large fluctuations and rapid changes in the deformation rate from 0 m to 250 m and from 850 m to 1500 m. The subsidence rate at Baisha Five Road Station and Qingling Station exceeded 35 mm/yr, with the maximum settlement reaching 70 mm, and other areas were relatively stable.

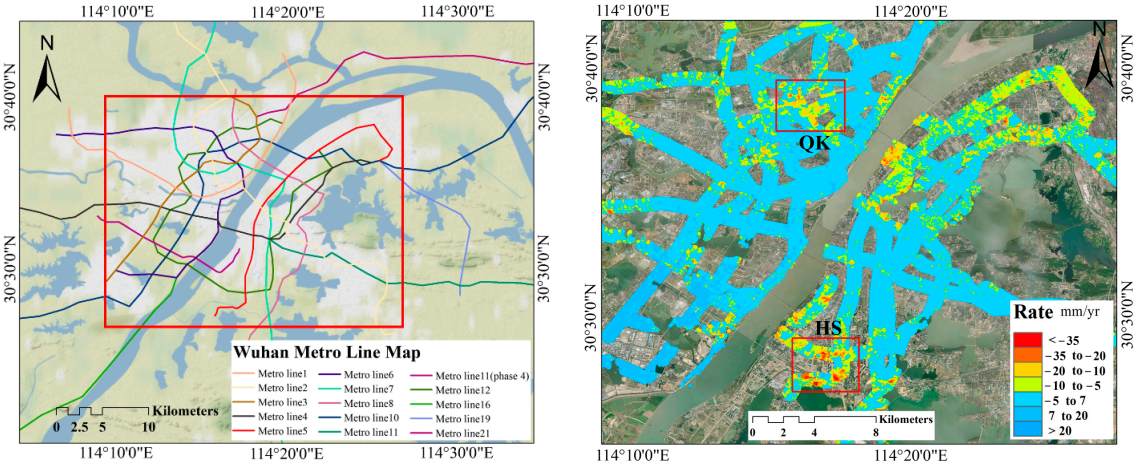

Figure 10. (**a**) Distribution of major metro lines in Wuhan; (**b**) land subsidence within 500 m on two sides of Wuhan subway. The red rectangle indicates the typical subsidence areas. JA and HS are the abbreviations of Jiangan and Hongshan, respectively. The red box in (**a**) indicates the range of optical satellite images.

Table 3. Information of Wuhan Metro under construction during the study period.

Name	Starting Point	End Point	Mileage	Construction Time
Metro Line 5	Hubei University of Chinese Medicine Station	East Square of Wuhan Railway Station	32.5 km	3 December 2015–10 December 2021
Metro Line 6	Jinyinhu Station	Xincheng 11th Road Station	7 km	28 July 2017–19 March 2021
Metro Line 12	Qingling Station	Qingling Station	59.876 km	18 December 2017–2024
Metro Line 16	South International Expo Center Station	Zhoujiahe Station	33.1 km	December 2018–September 2021
Metro Line 19	Wuhan Railway Station	Gaoxin 2nd Road Station	23.3 km	19 February 2019–2023

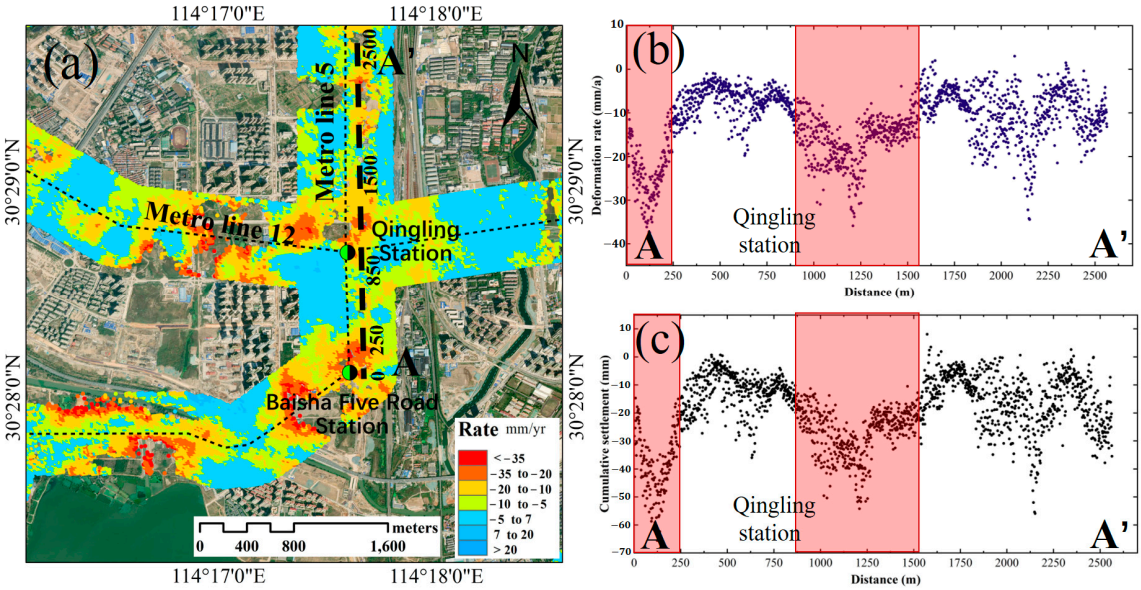

Figure 11. (**a**) Land subsidence along Qingling Station; (**b**) Deformation rate on profile AA′; (**c**) Cumulative settlement on profile AA′. The black dashed line AA′ is the profile position. The red boxes in (**b**,**c**) represent the subsidence intervals.

Shiqiao Station is also a typical area, and the subsidence is shown in Figure 12a. Two subsidence areas (S1 and S2) are found at the intersection of Metro Lines 6 and 12. Combined with the Google satellite optical images of the area, S1 is located in a residential neighborhood, and S2 is a vacant land. Residential buildings were being constructed in the S1 area during the study period. The simultaneous construction of subway and building leads to the subsidence of nearby ground. A 3D land subsidence model of S1 is shown in Figure 12c. The cumulative settlement in the study period reached 30 mm. We plotted the deformation rate and cumulative settlement profiles along BB'. The results are shown in Figure 12d,e. In a word, the subsidence fluctuation shows a "W" shape, with two obvious subsiding areas. The maximum settlement is located at S2, with a cumulative settlement of approximately 60 mm.

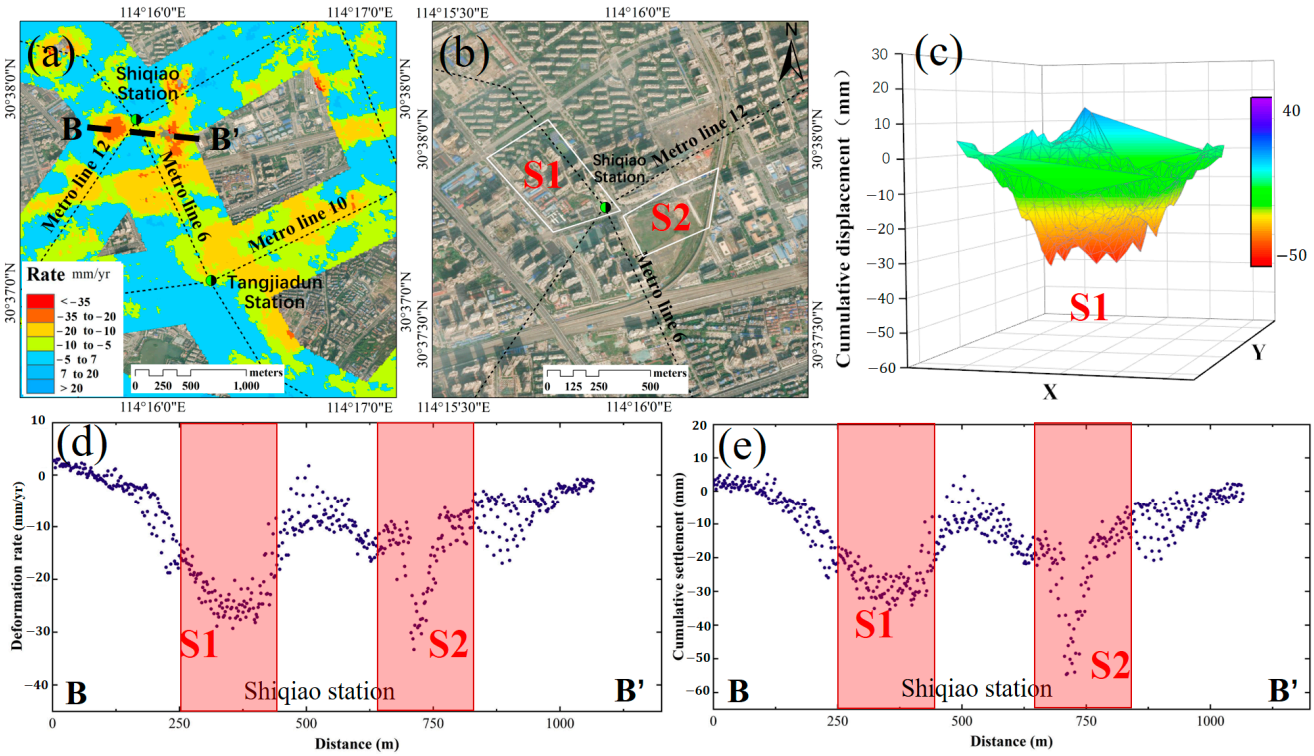

Figure 12. (**a**) Land subsidence around Shiqiao Station; (**b**) Google satellite optical images of the region; (**c**) three-dimensional land subsidence model of S1; (**d**) Deformation rate on profile BB'; (**e**) Cumulative settlement on profile BB'. The black dashed line BB' is the profile position. The white boxes in (**b**) indicates the location of the subsidence funnel. The red boxes in (**d**,**e**) represent the subsidence intervals.

5.2. Infrastructure Construction

Urban construction is also an important cause of land subsidence. As the central city of central China, Wuhan has made great development in urban infrastructure construction in recent years, starting from the construction of tall buildings, city ring road, rail transit, sponge city and other projects. Various construction projects in Wuhan resumed one after another after April 2020. Groundwater needs to be pumped during the excavation of the foundation pit before the construction of the building, and the construction of the building will increase the ground load, all of which may cause subsidence. Figure 13 shows the urban surface changes in four obvious subsidence areas in Wuhan during the study period. To further investigate the settlement trend in the surrounding area during the construction of the building, we selected some reference points in the center of the settlement area to draw the cumulative settlement curve. The results are shown in Figure 14.

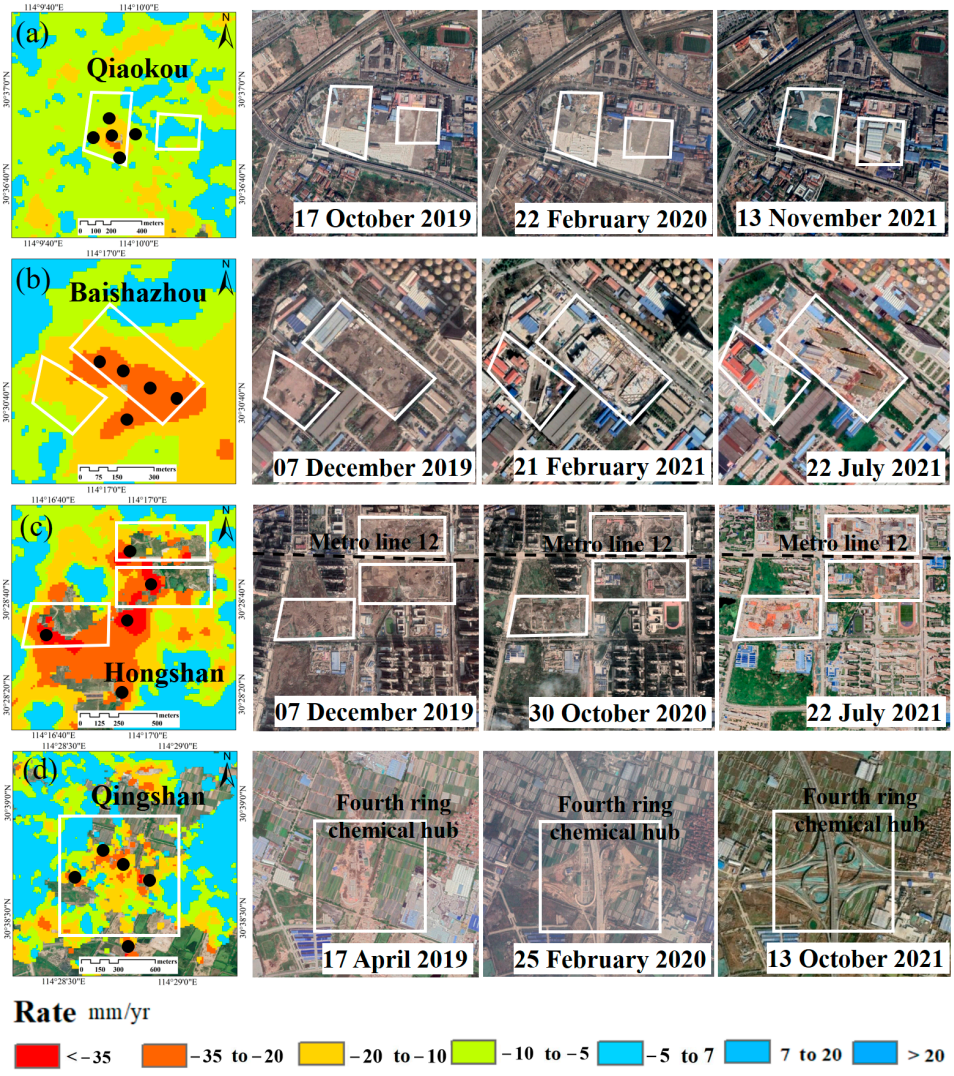

Figure 13. Urban surface changes in four obvious subsidence areas in Wuhan. The white boxes are the construction area. Black dots indicate the locations of the PS points.

Figure 13a shows an industrial park in Qiaokou District. The subsidence began to appear with the excavation of the foundation pit in September 2020, and the subsidence decreased after the construction of the foundation pit was completed in April 2021. Figure 13b shows a construction site located near Yangsigang Yangtze River Bridge in Baishazhou, where the construction of residential buildings was ongoing at the center of settlement during the study period. Figure 14b shows that subsidence continues until May 2021, with cumulative subsidence reaching about 50 mm. The rapid construction of high-rise buildings increases the ground load, which leads to the compression of soft soil layers and causes land subsidence.

In addition to a single building, multiple buildings are constructed in reality, which will cause regional large-scale subsidence. The subsidence in Hongshan District is shown in Figure 13c. Many office and residential buildings have been built near Qingling in Hongshan District in the past few years, and the area is close to Metro Lines 5 and 12 under construction. The simultaneous construction of the above ground part and the underground part has resulted in multiple subsidence funnels in this area. The optical image shows that the subsidence center is located at the people's Hospital of Wuhan University in Hongshan District under construction, and the maximum settlement exceeds 80 mm. Bridge construction can also cause land subsidence. Figure 13d shows a transportation hub under construction on the fourth ring road in Qingshan District. During the construction

of the bridge, significant land subsidence occurred in the surrounding area from June 2020. The overpass has been completed, and the cumulative settlement has reached 40 mm until September 2021. The spatial distribution of land subsidence in Wuhan is affected by urban construction to a certain extent.

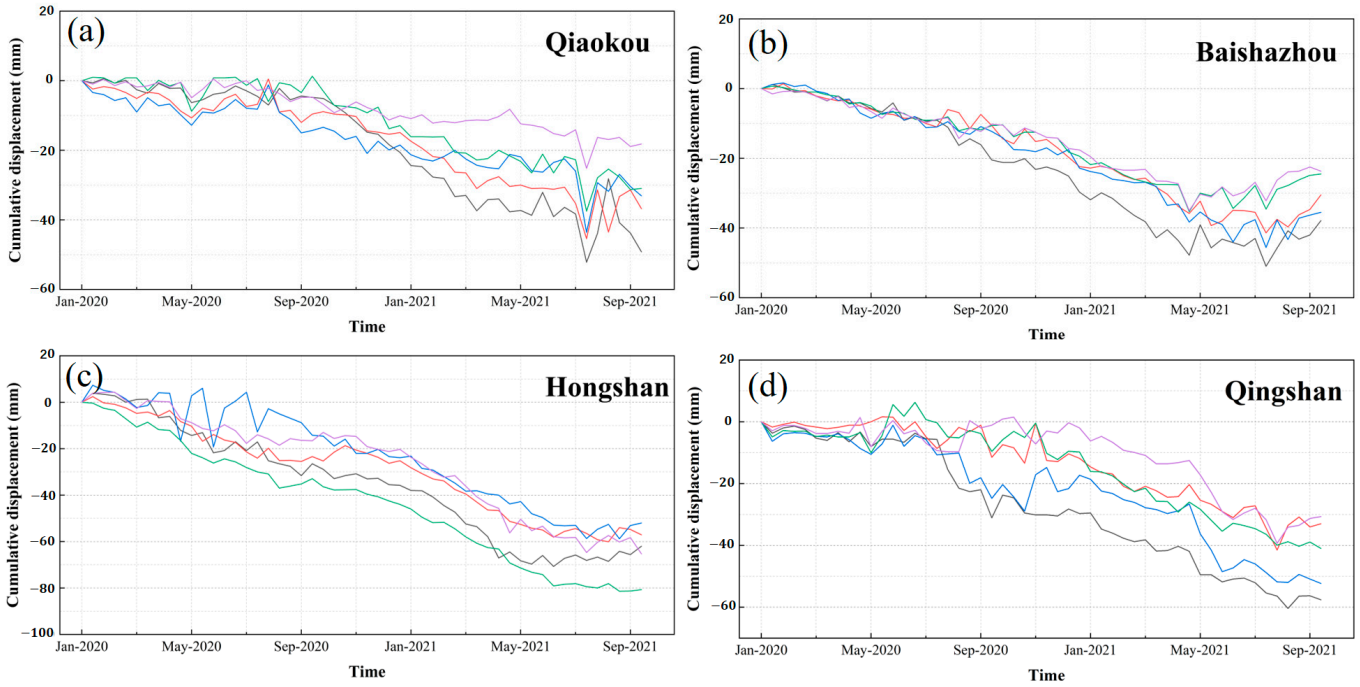

Figure 14. (**a**) Cumulative settlement curve of subsidence areas in Qiaokou District; (**b**) Cumulative settlement curve of subsidence areas in Baisahzhou; (**c**) Cumulative settlement curve of subsidence areas in Hongshan District; (**d**) Cumulative settlement curve of subsidence areas in qingshan District. Lines of different colors indicate the change in the subsidence of PS points.

5.3. Influence of Hydrogeology on Land Subsidence

Wuhan has complex geological conditions, carbonate rocks and soft soils are widely distributed, and special soils, such as artificial fill layers and old clay, are found. Figure 15a illustrates the spatial relationship between land subsidence and carbonate rock and soft soil. Most of the subsidence areas are located on carbonate rock and soft soil layer. For example, HH and QS are located on soft soil layer, and HS is located in carbonate rock belt and soft soil superposition area. Soft soils have high water content and low bearing capacity, and construction in areas with thick layers of soft soils can easily cause subsidence. Excessive groundwater extraction in large-scale urban construction can lead to a significant drop in the water level of fractured karst. The rapid change in karst groundwater dynamics gradually destroys the soil structure and forms soil cavities, leading to karst collapse of the ground. The special geological conditions of Wuhan make the city highly susceptible to geological hazards. We counted some of the locations of subsidence and ground collapse hazards recorded in Wuhan city, as shown in Figure 15b. Since 1977, about 30 karst collapse events have occurred in the Baishazhou carbonate belt in Hongshan District, and several subsidence disasters have occurred in the Houhu and Wuchang areas. However, the subsidence is only concentrated in a small part of the area, most of the areas located in carbonate rock or soft soil areas have relatively stable ground surface, and the land subsidence is insignificant. Areas located in carbonate rocks or soft soils do not necessarily experience land subsidence but are more likely to experience subsidence. Therefore, hydrogeology is not a decisive factor in the formation of subsidence.

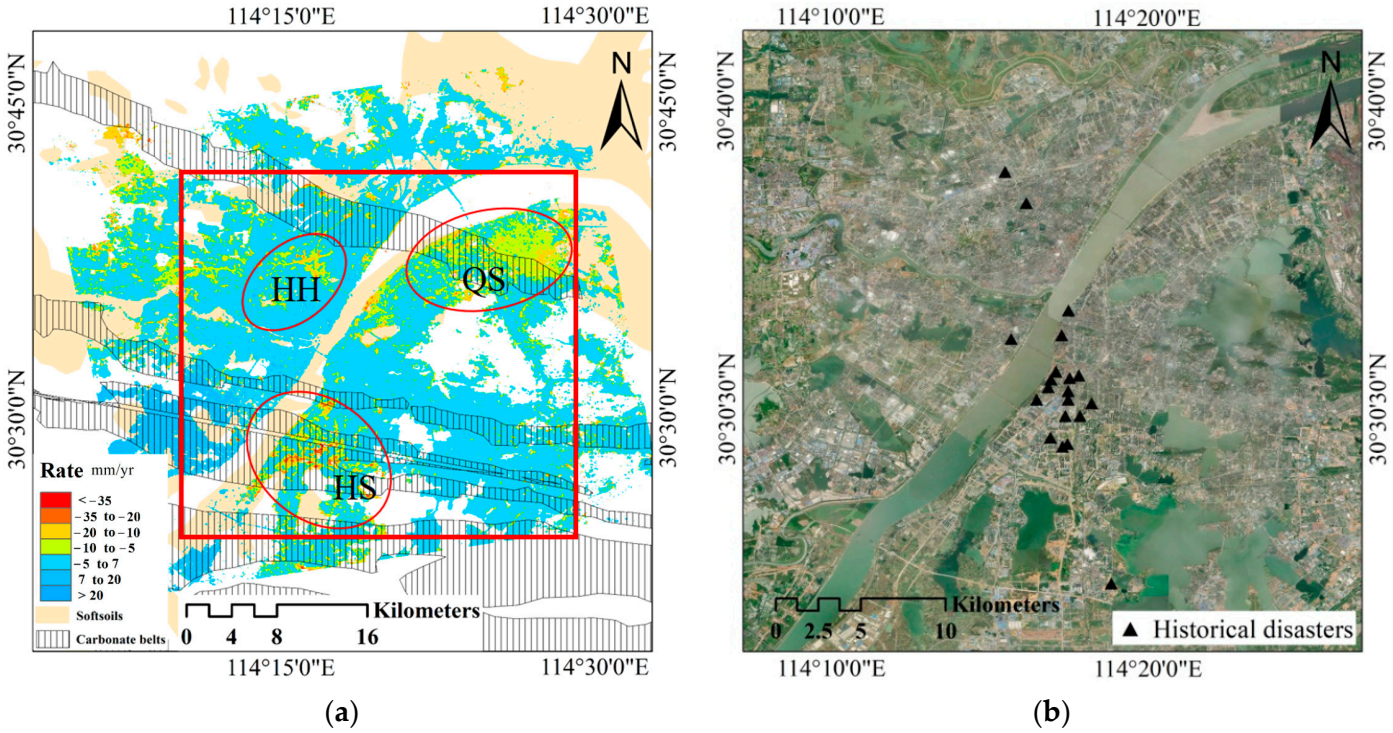

Figure 15. (**a**) Spatial relationship between land subsidence and carbonate rocks and soft soils in Wuhan; (**b**) location of subsidence and ground collapse disaster sites in Wuhan. The red ellipse in (**a**) indicates the subsidence area. HH, QS and HS are the abbreviations of Houhu, Qingshan, and Hongshan, respectively. The red rectangle in (**a**) indicates the range of optical satellite images.

5.4. Impact of Groundwater and Rainfall on Land Subsidence

An important factor in ground subsidence is the excessive extraction of groundwater. Figure 16a shows the changes in total water resources and average annual rainfall in Wuhan between 2015 and 2020. After 2016, the annual rainfall and the total amount of water resources in Wuhan decrease, and this situation is not improved until 2020. The proportional distribution of water consumption in Wuhan in 2020 is shown in Figure 16b, with industry and agriculture accounting for the largest share of water consumption. Qingshan District is a heavy industrial area and an important national steel production and chemical base. Many large industrial parks are located in this area as shown in Figure 16c. The groundwater in Qingshan District is mainly pore pressurized water in the loose accumulation layer, which is distributed in a band. One possible cause of the widespread ground subsidence phenomenon in the Qingshan district is the over exploitation of groundwater in industrial production.

To analyze the relationship between rainfall and land subsidence, we selected 15 reference points in different areas of Wuhan and compared the cumulative ground subsidence at the reference points with the monthly rainfall during the study period. The results are shown in Figure 16d. Rainfall in Wuhan is concentrated from May to September each year, with less rainfall in other months. The trend of ground deformation in Wuhan is associated with the rainfall in a certain time range. A large increase in rainfall is observed in Wuhan between May and September 2020, after which the deformation rate decreases in all subsiding areas, with some areas of slight ground uplift. After September, rainfall decreases significantly, and the rate of ground subsidence begins to increase. The results indicate a link between the magnitude of rainfall and land subsidence. In the time range of large rainfall, the land subsidence decreases, showing that a large amount of rainfall can effectively recharge groundwater resources and reduce the rate of surface subsidence.

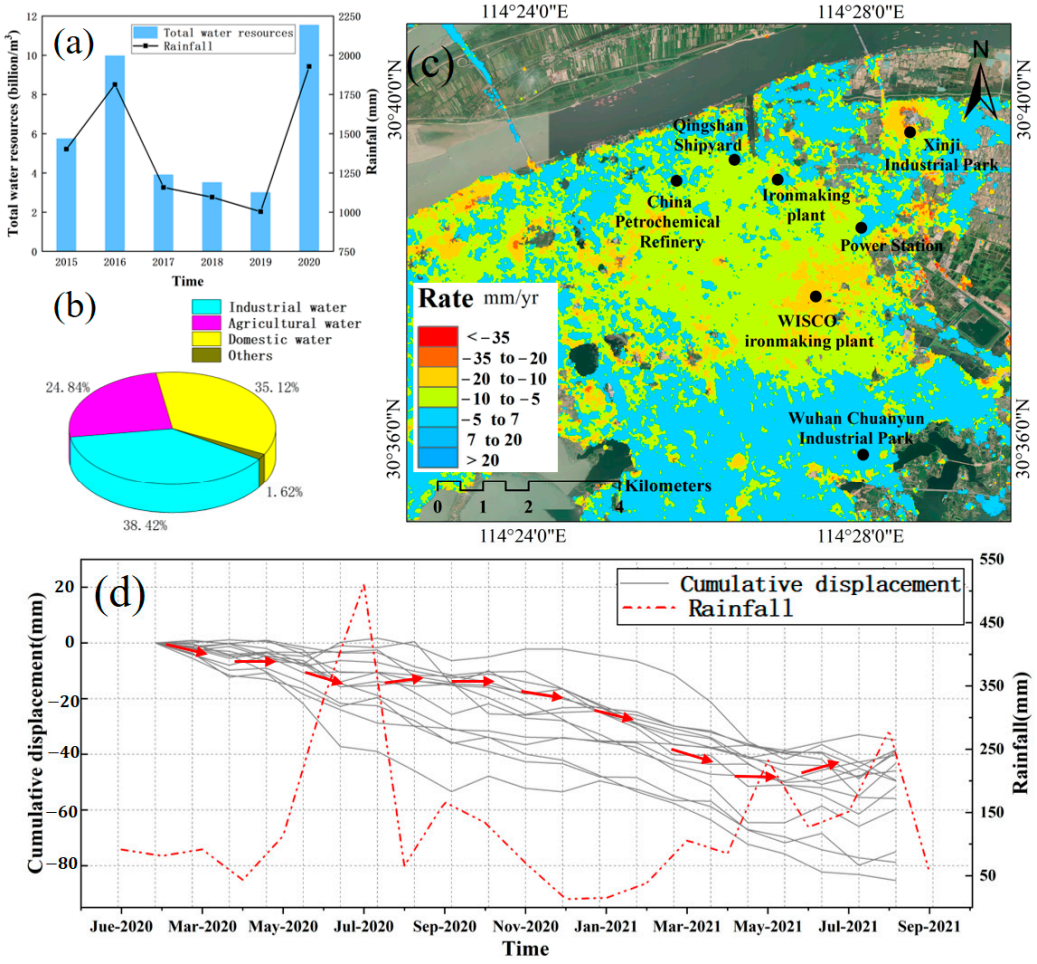

Figure 16. (**a**) Changes in total water resources and average annual rainfall in Wuhan between 2015 and 2020; (**b**) proportional distribution of water consumption in Wuhan in 2020; (**c**) distribution of industrial parks in Qingshan District; (**d**) comparison between cumulative subsidence and monthly rainfall in Wuhan. The red arrow indicates the change trend of subsidence.

5.5. Relationship between River Water Level Change and Land Subsidence

Wuhan is known as the "City of a Hundred Lakes", where the Yangtze River and Han River meet and form a water network together with many lakes. The total water area is 2117.6 km^2. The change in river water level is easy to lead to flood disaster, which affects the urban construction and people's normal lives in Wuhan. In 2020, Wuhan flood precipitation accounted for 75.8% of the annual precipitation. The Yangtze River passed through five flood peaks, and the water level of Hankou station was up to 28.77 m. Changes in water levels bring disasters and affect the ground stability along the rivers in Wuhan. The subsidence along the Han River in Qiaokou District (Figure 17b) and along the Yangtze River Road in Wuchang District (Figure 17c) may be related to water level changes. Several carbonate belts in Wuhan cross the Yangtze River, and the underground aquifers are connected to the Yangtze River. The change in water level leads to groundwater infiltration into the carbonate rock, which erodes and dissolves the carbonate rock causing more ground subsidence or collapse.

We selected two observation stations located in the Hankou area of the Yangtze River and the Hanchuan area of the Han River, respectively, and recorded the changes in water level at the stations during the study period. The locations of the stations are shown in Figure 17a. The water level changes at the two stations are the same, and the water level changes considerably during the flood season. Figure 17d,e show the relationship between water level values and land subsidence at the two observation stations of Yangtze and Han

Rivers, respectively. The peaks presented in water level changes and subsidence changes have some similarity, but the peaks in the cumulative deformation time series appear later than the water level changes. The subsidence decreases with the increase in the water level of the Yangtze River from May 2020, and the cumulative subsidence increases with the decrease in the water level of the Yangtze River after September 2020. The subsidence in areas farther away from the Han River is less influenced by the water level, and the correlation between the subsidence trend and the water level change is small. The closer to the water surface, the more similar the cumulative deformation curve is to the water level. There may be a link between land subsidence and water level changes on two sides of the Yangtze River. However, the seasonal variation of subsidence time series cannot be studied in detail due to insufficient data and short study period. More data will be used in future studies to further determine the correlation between land subsidence and water level changes.

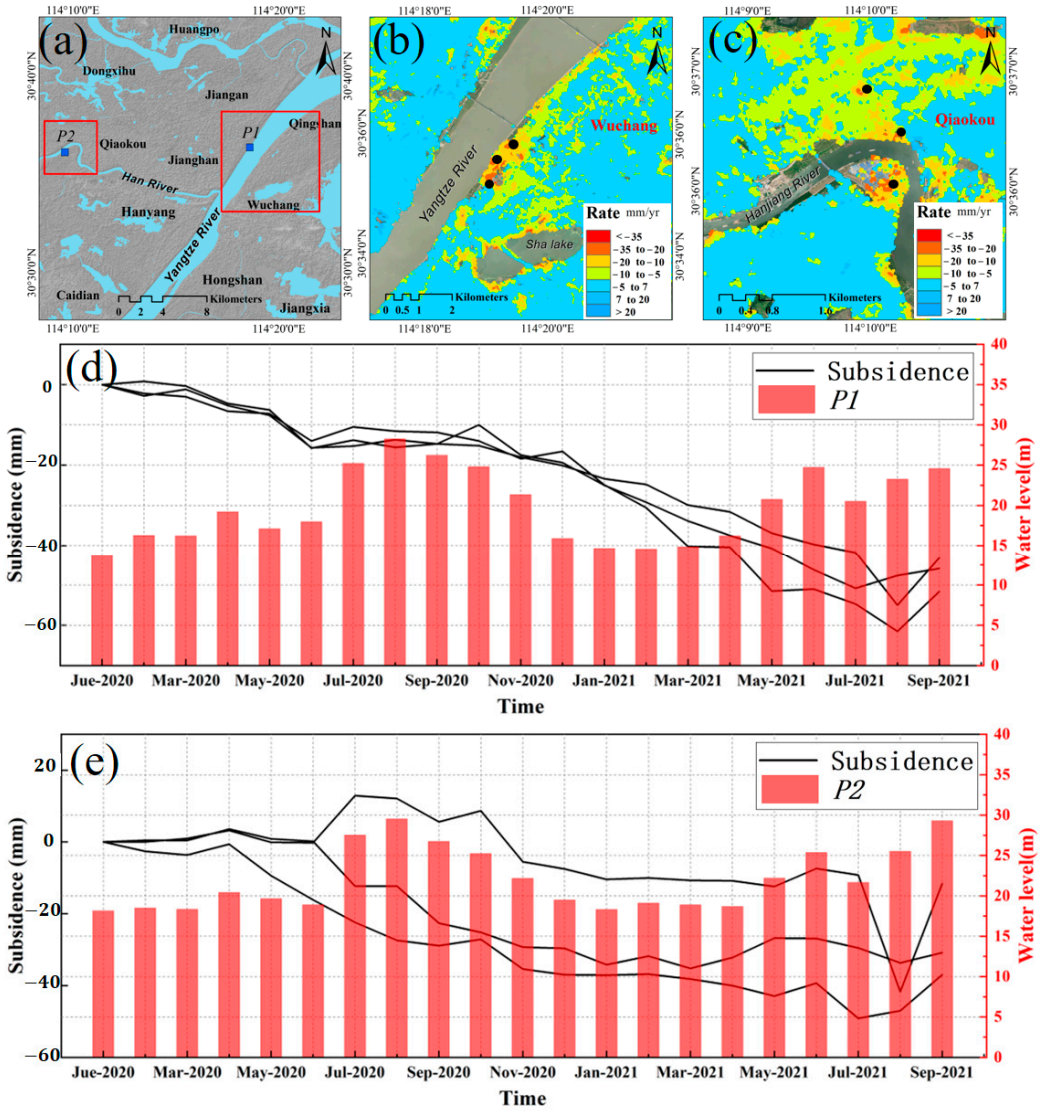

Figure 17. (**a**) Location of observation station; (**b**) subsidence along Changjiang Road in Wuchang District; (**c**) subsidence along the Han River in Qiaokou District; (**d**) comparison of water level and land subsidence in the Yangtze River; (**e**) comparison of water level and land subsidence in the Han River. P1 and P2 indicate the location of the observation point. The red boxes indicate the ranges of (**b**) and (**c**), respectively. Black dots indicate reference point locations.

5.6. Ground Uplift in Wuhan

In the result map of InSAR, the subsidence information of the ground surface can be extracted and the uplift information can be found. Although the main deformation of Wuhan is subsidence, it has significant uplift. As shown in Figure 18a, the uplift phenomenon is mainly concentrated in Caidian District in the south of Wuhan, with uplift rates ranging from 10 mm/yr to 20 mm/yr, and uplift exists in the downtown area. Dozens of lakes are located in Caidian District (Figure 18b), groundwater is abundant, and urban construction activities are low, so subsidence rarely occurs. Silty clay, muddy silty clay and old clay are widely distributed in Wuhan. The old clay is rich in expansive clay minerals, such as montmorillonite and illite. They produce physical and chemical swelling effects when they encounter water, resulting in volume expansion. Geological tectonics, flood deposition of the Yangtze River, and artificial filled soil are factors affecting the ground uplift in Wuhan [50]. At present, no clear explanation is provided for the phenomenon of ground lifting in Wuhan, and further research is still needed.

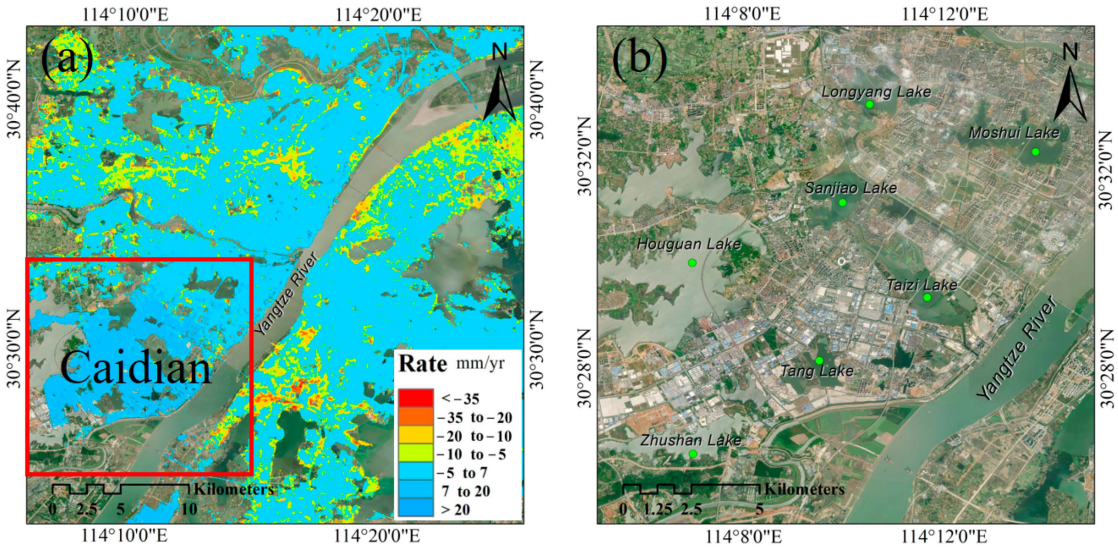

Figure 18. (**a**) Ground uplift in Wuhan city; (**b**) location distribution of major lakes in Caidian District. The green dots indicate lakes. The red box indicates the range of optical satellite images.

6. Conclusions

In this paper, we used 80 Sentinel-1A (SAR) images covering Wuhan to obtain the land subsidence information of Wuhan from July 2017 to September 2021 with the SBAS-InSAR technique. In accordance with the temporal and spatial distribution characteristics of land subsidence in Wuhan, we explored the causes of land subsidence in Wuhan in combination with subway association, infrastructure construction, hydrogeology, groundwater and rainfall, and changes in river water level. We briefly discussed the phenomenon of ground uplift in Caidian District.

The results show that the land subsidence in Wuhan is not uniformly distributed, with a maximum subsidence rate of 57.08 mm/yr. The subsidence funnel is distributed in the area covered by a soft soil layer and carbonate rock belt. Compared with that before 2017, the subsidence of Houhu area in Wuhan is obviously smaller. In contrast, the subsidence in other areas is severe. At present, the major subsidence areas in Wuhan are Jiangan, Qiaokou, Qingshan, Wuchang and Hongshan Districts. The subsidence near Qingling is the most serious, with a maximum cumulative deformation of 90 mm. The subsidence extend in this area is expanding, and multiple subsidence funnels tend to be connected.

Urban development and engineering construction are the major factors causing land subsidence in Wuhan. The construction of large buildings and subways increases the ground load, disturbs the surrounding soil and affects the ground stability, resulting in

subsidence. Special geological formations are an important factor in land subsidence in Wuhan. Carbonate rock belts and large areas of soft soils make Wuhan more prone to geological problems such as karst ground collapse and uneven foundation subsidence. The amount of rainfall affects the total amount of water resources and changes in the water level of the Yangtze River. A large amount of rainfall in flood season can recharge groundwater resources and reduce the rate of land subsidence. The change in river water level has a certain impact on the land subsidence along the river in Wuhan, but the impact is small.

An obvious uplift is observed in Caidian District, and the reason for the uplift may be related to the physical expansion and chemical expansion effects of the old clay. At present, the type and accuracy of radar data continue to improve with the launch of more SAR satellites, thereby helping to better monitor urban subsidence, identify potential risks and delve into the mechanisms of subsidence.

Author Contributions: Y.Z., J.L. and L.Z. conceived and designed the experiments; C.W., J.Q. and H.S. carried out the data acquisition; Y.Z. and L.Z. performed data processing and analyses, and X.L. contributed to the manuscript of the paper; Y.Z., L.Z. and L.H. discussed and analyzed the experimental results. All authors have read and agreed to the published version of the manuscript.

Funding: This work was supported by the Guangxi Science and Technology Plan Project (Grant Nos. GUIKE AD19110107 and GUIKE AD19245060); the National Natural Science Foundation of China (Grant No. 42064002); the Natural Science Foundation of Guangxi (Grant No. 2020GXNSFBA159033); and the Guangxi Spatial Information Key Laboratory of Surveying and Mapping (Grant No. 19-185-10-05).

Data Availability Statement: Data incorporated in this research is available free through the these webpages: Sentinel-1A (https://scihub.copernicus.eu/dhus/#/home, accessed on 20 December 2021), SRTM DEM (http://srtm.csi.cgiar.org/srtmdata, accessed on 24 December 2021), satellite precise orbit data (https://qc.sentinel1.eo.esa.int/aux_poeorb, accessed on 29 December 2021).

Acknowledgments: We are grateful to the European Space Agency for providing the Sentinel-1A data and POD data for free. We would also like to thank NASA for providing the SRTM3 DEM data.

Conflicts of Interest: The authors declare no conflict of interest.

References

1. Cigna, F.; Tapete, D. Present-day land subsidence rates, surface faulting hazard and risk in Mexico City with 2014–2020 Sentinel-1 IW InSAR. *Remote Sens. Environ.* **2021**, *253*, 112161. [CrossRef]
2. Fedeski, M.; Gwilliam, J. Urban sustainability in the presence of flood and geological hazards: The development of a GIS-based vulnerability and risk assessment methodology. *Landsc. Urban Plan.* **2007**, *83*, 50–61. [CrossRef]
3. Wang, R.; Yang, T.; Yang, M.; Liao, M.; Lin, J.; Zhang, L. Attribution Analysis on Deformation Feature of the Shanghai Elevated Highway by Persistent Scatterer SAR Interferometry. *Geomat. Inf. Sci. Wuhan Univ.* **2018**, *43*, 2050–2057.
4. Agarwal, V.; Kumar, A.; Gee, D.; Grebby, S.; Gomes, R.L.; Marsh, S. Comparative Study of Groundwater-Induced Subsidence for London and Delhi Using PSInSAR. *Remote Sens.* **2021**, *13*, 4741. [CrossRef]
5. Zhang, X.; Chen, B.; Gong, H.; Lei, K.; Zhou, C.; Lu, Z.; Zhao, D. Inversion of Groundwater Storage Variations Considering Lag Effect in Beijing Plain, from RadarSat-2 with SBAS-InSAR Technology. *Remote Sens.* **2022**, *14*, 991. [CrossRef]
6. Najafabadi, R.; Ramesht, M.; Ghazi, I.; Khajedin, S.; Seif, A.; Nohegar, A.; Mahdavi, A. Identification of natural hazards and classification of urban areas by TOPSIS model (case study: Bandar Abbas city, Iran). *Geomat. Nat. Hazards Risk* **2016**, *7*, 85–100. [CrossRef]
7. Teatini, P.; Ferronato, M.; Gambolati, G.; Gonella, M. Groundwater pumping and land subsidence in the Emilia-Romagna coastland, Italy: Modeling the past occurrence and the future trend. *Water Resour. Res.* **2006**, *42*. [CrossRef]
8. El Bastawesy, M.; Cherif, O.; Sultan, M. The geomorphological evidences of subsidence in the Nile Delta: Analysis of high resolution topographic DEM and multi-temporal satellite images. *J. Afr. Earth Sci.* **2017**, *136*, 252–261. [CrossRef]
9. Bonì, R.; Herrera, G.; Meisina, C.; Notti, D.; Béjar-Pizarro, M.; Zucca, F.; González, P.; Palano, M.; Tomás, R.; Fernández, J.; et al. Twenty-year advanced DInSAR analysis of severe land subsidence: The Alto Guadalentín Basin (Spain) case study. *Eng. Geol.* **2015**, *198*, 40–52. [CrossRef]
10. Herrera, G.; Fernández, J.; Tomás, R.; Cooksley, G.; Mulas, J. Advanced interpretation of subsidence in Murcia (SE Spain) using A-DInSAR data-modelling and validation. *Nat. Hazards Earth Syst. Sci.* **2009**, *9*, 647–661. [CrossRef]
11. Chaussard, E.; Wdowinski, S.; Cabral-Cano, E.; Amelung, F. Land subsidence in central Mexico detected by ALOS InSAR time-series. *Remote Sens. Environ.* **2014**, *140*, 94–106. [CrossRef]
12. Qu, F.; Lu, Z.; Zhang, Q.; Bawden, G.; Kim, J.; Zhao, C.; Qu, W. Mapping ground deformation over Houston–Galveston, Texas using multi-temporal InSAR. *Remote Sens. Environ.* **2015**, *169*, 290–306. [CrossRef]

13. Ng, A.; Ge, L.; Li, X.; Abidin, H.; Andreas, H.; Zhang, K. Mapping land subsidence in Jakarta, Indonesia using persistent scatterer interferometry (PSI) technique with ALOS PALSAR. *Int. J. Appl. Earth Obs.* **2012**, *18*, 232–242. [CrossRef]
14. Zhu, L.; Gong, H.; Li, X.; Wang, R.; Chen, B.; Dai, Z.; Teatini, P. Land subsidence due to groundwater withdrawal in the northern Beijing plain, China. *Eng. Geol.* **2015**, *193*, 243–255. [CrossRef]
15. Qu, F.; Zhang, Q.; Lu, Z.; Zhao, C.; Yang, C.; Zhang, J. Land subsidence and ground fissures in Xi'an, China 2005–2012 revealed by multi-band InSAR time-series analysis. *Remote Sens. Environ.* **2014**, *155*, 366–376. [CrossRef]
16. Gao, M.; Gong, H.; Li, X.; Chen, B.; Zhou, C.; Shi, M.; Guo, L.; Chen, Z.; Ni, Z.; Duan, G. Land Subsidence and Ground Fissures in Beijing Capital International Airport (BCIA): Evidence from Quasi-PS InSAR Analysis. *Remote Sens.* **2019**, *11*, 1466. [CrossRef]
17. Gerardo, H.; Pablo, E.; Roberto, T.; Marta, B.; Juan, L.; Mauro, R.; Maria, M.; Dora, C.; John, L.; Pietro, T.; et al. Mapping the global threat of land subsidence. *Science* **2021**, *371*, 34–36.
18. Hu, R.; Yue, Z.; Wang, L.; Wang, S. Review on current status and challenging issues of land subsidence in china. *Eng. Geol.* **2004**, *76*, 65–77. [CrossRef]
19. Zhang, T.; Shen, W.-B.; Wu, W.; Zhang, B.; Pan, Y. Recent Surface Deformation in the Tianjin Area Revealed by Sentinel-1A Data. *Remote Sens.* **2019**, *11*, 130. [CrossRef]
20. Xiang, W.; Zhang, R.; Liu, G.; Wang, X.; Mao, W.; Zhang, B.; Cai, J.; Bao, J.; Fu, X. Extraction and analysis of saline soil deformation in the Qarhan Salt Lake region (in Qinghai, China) by the sentinel SBAS-InSAR technique. *Geod. Geodyn.* **2022**, *13*, 127–137. [CrossRef]
21. Du, Y.; Feng, G.; Liu, L.; Fu, H.; Peng, X.; Wen, D. Understanding Land Subsidence Along the Coastal Areas of Guangdong, China, by Analyzing Multi-Track MTInSAR Data. *Remote Sens.* **2020**, *12*, 299. [CrossRef]
22. Liu, Q.; Yue, G.; Ding, X.; Yang, K.; Feng, G.; Xiong, Z. Temporal and Spatial Characteristics Analysis of Deformation Along Foshan Subway Using Time Series InSAR. *Geomat. Inf. Sci. Wuhan Univ.* **2019**, *44*, 1099–1106.
23. Li, W.; Wang, L.; Guo, H.; Wang, H.; Wang, Y.; Zhu, J.; Zang, X. Effectiveness and countermeasures of land subsidence control in China. *China Water Resour.* **2021**, *7*, 32–35.
24. Huang, J.; Guo, Y.; Luo, W. Monitoring land subsidence in Wuhan city based on Sentinel-1. *Bull. Surv. Map.* **2021**, *9*, 53–58.
25. Hu, J.; Motagh, M.; Wang, J.; Qin, F.; Zhang, J.; Wu, W.; Han, Y. Karst Collapse Risk Zonation and Evaluation in Wuhan, China Based on Analytic Hierarchy Process, Logistic Regression, and InSAR Angular Distortion Approaches. *Remote Sens.* **2021**, *13*, 5063. [CrossRef]
26. Fan, S. A Discussion on Karst Collapse in Wuhan (Hubei). *Resour. Environ. Eng.* **2006**, *20*, 608–616.
27. Benattou, M.; Balz, T.; Liao, M. Measuring Surface Subsidence in Wuhan, China with Sentinel-1 Data using PSInSAR. *Int. Arch. Photogramm. Remote Sens. Spat. Inf. Sci.* **2018**, *XLII-3*, 73–77. [CrossRef]
28. Jiang, H.; Balz, T.; Cigna, F.; Tapete, D. Land Subsidence in Wuhan Revealed Using a Non-Linear PSInSAR Approach with Long Time Series of COSMO-SkyMed SAR Data. *Remote Sens.* **2021**, *13*, 1256. [CrossRef]
29. Guo, J.; Zhou, L.; Yao, C.; Hu, J. Surface Subsidence Analysis by Multi-Temporal InSAR and GRACE: A Case Study in Beijing. *Sensors* **2016**, *16*, 1495. [CrossRef]
30. Wu, C. Research and Analysis on the Subsidence of Houhu Real Estate in Wuhan. *Technol. Inno. Appl.* **2014**, *22*, 216.
31. Han, Y.; Zou, J.; Lu, Z.; Qu, F.; Kang, Y.; Li, J. Ground Deformation of Wuhan, China, Revealed by Multi-Temporal InSAR Analysis. *Remote Sens.* **2020**, *12*, 3788. [CrossRef]
32. Zhou, L.; Lu, J.; Wen, X.; Zhang, D.; Wang, C.; Yang, F. Spatial-temporal Characteristics Analysis of Ground Subsidence in Central Urban Areas of Wuhan Based on Small Baseline Subset lnterferometric Synthetic Aperture Radar. *Sci. Technol. Eng.* **2021**, *21*, 40–46.
33. Huang, B.; Zheng, F.; Bai, J.; Wang, Y. Feasibility of land surface deformation monitoring by regional CORS. *J. Geomat. Sci. Technol.* **2011**, *28*, 169–172.
34. Chen, Q.; Liu, G.; Hu, Z.; Ding, X.; Yang, Y. Mapping ground 3-D displacement with GPS and PS-InSAR networking in the Pingtung area, southwestern Taiwan. *Chin. J. Geophys.* **2012**, *55*, 3248–3258.
35. Hooper, A. A multi-temporal InSAR method incorporating both persistent scatterer and small baseline approaches. *Geophys. Res. Lett.* **2008**, *35*, 96–106. [CrossRef]
36. Chaussard, E.; Amelung, F.; Abidin, H.; Hong, S. Sinking cities in Indonesia: ALOS PALSAR detects rapid subsidence due to groundwater and gas extraction. *Remote Sens. Environ.* **2013**, *128*, 150–161. [CrossRef]
37. Zhu, J.; Yang, Z.; Li, Z. Recent progress in retrieving and predicting mining-induced 3D displacements using InSAR. *Acta Geod. Cartogr. Sin.* **2019**, *48*, 135–144. [CrossRef]
38. Karanam, V.; Motagh, M.; Garg, S.; Jain, K. Multi-sensor remote sensing analysis of coalfire induced land subsidence in Jharia Coalfields, Jharkhand, India. *Int. J. Appl. Earth Obs. Geoinf.* **2021**, *102*, 102439.
39. Liu, Z.; Xu, B.; Wang, Q.; Yu, W.; Miao, Z. Monitoring landslide associated with reservoir impoundment using synthetic aperture radar interferometry: A case study of the Yalong reservoir. *Geod. Geodyn.* **2022**, *13*, 138–150. [CrossRef]
40. Perissin, D.; Wang, Z.Y.; Lin, H. Shanghai subway tunnels and highways monitoring through cosmo-skymed persistent scatterers. *ISPRS J. Photogramm. Remote Sens.* **2012**, *73*, 58–67. [CrossRef]
41. Chen, G.; Zhang, Y.; Zeng, R.; Yang, Z.; Chen, X.; Zhao, F.; Meng, X. Detection of Land Subsidence Associated with Land Creation and Rapid Urbanization in the Chinese Loess Plateau Using Time Series InSAR: A Case Study of Lanzhou New District. *Remote Sens.* **2018**, *10*, 270. [CrossRef]

42. Pratesi, F.; Tapete, D.; Del Ventisette, C.; Moretti, S. Mapping interactions between geology, subsurface resource exploitation and urban development in transforming cities using insar persistent scatterers: Two decades of change in Florence, Italy. *Appl. Geogr.* **2016**, *77*, 20–37. [CrossRef]
43. Ferretti, A.; Prati, C.; Rocca, F. Permanent scatterers in SAR interferometry. *IEEE Trans. Geosci. Remote Sens.* **2001**, *39*, 8–20. [CrossRef]
44. Beradino, P.; Fornaro, G.; Lanari, R.; Sansosti, E. A new algorithm for Surface deformation monitoring based on small baseline differential SAR interferograms. *IEEE Trans. Geosci. Remote Sens.* **2002**, *40*, 2375–2383. [CrossRef]
45. Li, J.H.; Zhou, L.; Ren, C.; Liu, L.L.; Zhang, D.; Shi, Y.J. Spatiotemporal Inversion and Mechanism Analysis of Surface Subsidence in Shanghai Area Based on Time-Series InSAR. *Appl. Sci.* **2021**, *11*, 7460. [CrossRef]
46. Bai, L.; Jiang, L.M.; Wang, H.S.; Sun, Q.S. Spatiotemporal characterization of land subsidence and uplift (2009–2010) over wuhan in central China revealed by terrasar-x insar analysis. *Remote Sens.* **2016**, *8*, 350. [CrossRef]
47. Costantini, M.; Bai, J.; Malvarosa, F.; Minati, F.; Vecchioli, F.; Wang, R.; Hu, Q.; Xiao, J.; Li, J. Ground deformations and building stability monitoring by COSMO-SkyMed PSP SAR interferometry: Results and validation with field measurements and surveys. In Proceedings of the 2016 IEEE International Geoscience and Remote Sensing Symposium (IGARSS), Beijing, China, 10–15 July 2016; pp. 6847–6850.
48. Zhou, L.; Guo, J.; Hu, J.; Li, J.; Xu, Y.; Pan, Y.; Shi, M. Wuhan Surface Subsidence Analysis in 2015–2016 Based on Sentinel-1A Data by SBAS-InSAR. *Remote Sens.* **2017**, *9*, 982. [CrossRef]
49. Zhang, Y.; Liu, Y.; Jin, M.; Jing, Y.; Liu, Y.; Liu, Y.; Sun, W.; Wei, J.; Chen, Y. Monitoring Land Subsidence in Wuhan city (China) using the SBAS-InSAR Method with Radarsat-2 Imagery Data. *Sensors* **2019**, *19*, 743. [CrossRef]
50. Xie, P.; Zhang, S.; Zhou, L.; Li, Q.; Xiao, J.; Cai, J. Detection of the Urban Surface Deformation and New Strategy for Flood Prevention in Wuhan Central District. *Geomat. Inf. Sci. Wuhan Univ.* **2021**, *46*, 1015–1024.
51. Shi, X.; Zhang, S.; Jiang, M.; Pei, Y.; Yang, C. Spatial and temporal subsidence characteristics in Wuhan city (China) during 2015–2019 inferred from Sentinel-1 SAR Interferometry. *Nat. Hazards Earth Syst. Sci.* **2021**, *21*, 2285–2297. [CrossRef]
52. Wang, Y.; Wu, J.; Wang, H.; Zhao, D. The statistical analysis of rainfall in wuhan in the past 50 years. *J. Hubei Univ. Technol.* **2006**, *21*, 98–100.
53. Zhao, Q.; Liu, Y.; Yao, W.; Yao, Y. Hourly Rainfall Forecast Model Using Supervised Learning Algorithm. *IEEE Trans. Geosci. Remote* **2021**, *99*, 4100509. [CrossRef]
54. Luo, X. Division of "six belts and five types" of carbonate region and control of karst geological disaster in Wuhan. *J. Hydraul. Eng.* **2014**, *45*, 171–179.